buildings

MDPI

Article

Experiments and Numerical Simulations on the Seismic Performance of Steel-Frame Composite Wallboard Shear Walls

Zhen Wang [1], Zhe Liu [2,3,*], Jia-Bao Yan [4,*], Xiao Ju [5] and Lei Han [6]

1 School of Transportation and Civil Engineering, Shandong Jiaotong University, Jinan 250357, China
2 School of Civil Engineering, Shandong Jianzhu University, Jinan 250101, China
3 Shandong Winbond Construction Group Co., Ltd., Weifang 262500, China
4 School of Civil Engineering, Tianjin University, Tianjin 300350, China
5 Jinan Rail Transportation Group Co., Ltd., Jinan 250014, China
6 School of Architecture and Engineering, Shandong University of Engineering and Vocational Technology, Jinan 250200, China
* Correspondence: liuzhe0624@126.com (Z.L.); ceeyanj@163.com (J.-B.Y.)

Abstract: In order to expand the applications of cold-formed thin-walled steel structures, this study proposes a new type of composite wallboard composed of cold-formed thin-walled C-shaped steel and multi-layer concrete, in which C-shaped steel serves as the skeleton, foam concrete acts as the thermal insulation material, and fine aggregate concrete and cement mortar play the part of envelopes. The composite wallboard can be made in a factory assembly line, meeting the requirements of the building (civil and structural) industry. Two steel-frame composite wallboard shear walls were subjected to reciprocating loading, with the connection mode as the design parameter, to investigate the seismic performance of the structure. The failure mode, hysteresis curve, skeleton curve, strength degradation, stiffness degradation, ductility, and energy dissipation capacity of the specimens were analyzed. On this basis, the finite element (FE) model of the steel-frame composite wallboard was established, and the model's accuracy was verified by comparing the bearing capacity and the skeleton curve. Results show that the structure shows shear failure characteristics, and the cement mortar layer and the fine aggregate concrete layer are separated from the C-shaped steel after being crushed. The infilled foam concrete is also crushed, and the welding seams between the extended C-shaped steel and steel frame of the WP-1 specimen are damaged. The hysteresis curves of the two specimens have a clear pinch, but the area enclosed by the hysteresis loop is large, and the energy dissipation capacity is also present. The yield load and ultimate load of the WP-2 specimen are higher than those of the WP-1 specimen, indicating that the higher the connection strength between the composite wallboard and the steel frame, the greater the ultimate carrying capacity of the specimen. The established FE model can accurately estimate the seismic performance of steel-frame composite wallboard shear walls.

Keywords: seismic performance; composite wallboard; cold-formed thin-walled steel; finite element model

Citation: Wang, Z.; Liu, Z.; Yan, J.-B.; Ju, X.; Han, L. Experiments and Numerical Simulations on the Seismic Performance of Steel-Frame Composite Wallboard Shear Walls. *Buildings* **2023**, *13*, 282. https://doi.org/10.3390/buildings13020282

Academic Editor: Harry Far

Received: 29 December 2022
Revised: 13 January 2023
Accepted: 16 January 2023
Published: 18 January 2023

1. Introduction

Cold-formed thin-walled steel (CFS) structures are a novel type of structural system composed of cold-formed thin-walled steel frames and sheathing material. Self-drilling screws are used to connect the steel frame and the sheathing [1]. It has high strength, is lightweight, makes easy connections, has convenient installation and recyclability, and is widely used in low-rise buildings [2]. Ordinary sheathing materials include steel plates [3,4], fiber cement boards (FCBs) [5], gypsum wallboards (GWBs) [6], oriented strand boards (OSBs) [7], Bolivian magnesium boards (BMGs) [8], and calcium silicate boards (CSBs) [9].

Previous studies have demonstrated that the type of sheathing material significantly affects the mechanical performance of CFS structures. Therefore, the load-bearing perfor-

mance and seismic behavior of CFS cladded with different sheathing materials have been investigated in past studies. For instance, Attari [10] reported an experimental study on the seismic performance of six CFS shear walls with steel sheeting. The failure modes included stud local buckling and sheeting edge rupture. DaBreo et al. [11] explored the influence factor of CFS shear walls clad with flat steel under lateral and gravity loading and found that the sheathing connection pattern is directly related to performance. Mohebbi et al. [12] performed cyclic loading on six CFS shear walls cladded with GWBs and FCBs. The results showed that the cladding increased the specimens' lateral stiffness, shear strength, and energy dissipation capacity. Zeynalian and Ronagh [13] examined the failure modes of CFS walls sheathed by FCBs and estimated the seismic response modification factor. The screw connections significantly influenced the system's nonlinear behavior. In a series of monotonic experiments, Serrette et al. [14] and Liu et al. [15] evaluated the static performance of CFS walls sheathed with OSBs, GWBs, and other sheathing materials. They discovered that the failure of the walls resulted from screws pulling through the panel or screws breaking the edge of the panel. Karabulut and Soyoz [16] carried out cyclic loading tests on CFS shear panels sheathed with GWBs. The contribution of board type, steel thickness, screw spacing, and axial load on the hysteresis behavior of the specimen was examined. It was found that the specimen's ductility is mainly due to the connection screws between the board and the CSF frame. Abeysiriwardena and Mahendran [17] conducted full-scale standard fire tests on three CFS walls sheathed with GWBs and found that the stronger the out-of-plane constraint, the higher the fire resistance of the wallboard.

Recently, more environment-friendly and recyclable materials have been used as sheathing. Liu et al. [18] put expanded polystyrene boards or extruded polystyrene boards, two kinds of thermal and sound insulation materials, in the cavity of the CFS frame and sprayed lightweight mortar on both sides of the CFS frame. The test result showed that the slippage between the sprayed lightweight mortar and the CFS frame improved stiffness and restricted cracks. Straw boards are a reused material composed of plant straw and protective paper. Xu et al. [19] and Zhang et al. [20] wrapped straw boards on both sides of a CFS frame and investigated seismic behavior and axial performance, respectively. The cracking of the straw board made the wall express better ductility and energy absorption. Wu et al. [21] filled CFS walls with OSBs and GWBs with flue gas desulfurization gypsum, a type of industrial waste. The infilled gypsum and the sheathing materials made up most of the contributions to lateral stiffness, and the compressive failures of infilled gypsum and screw connection failure were both limited states.

In some studies, it was found that the failure modes of CFS shear walls with sheathing materials were the local buckling of the studs, the crushing of the sheathing, and self-scraw failure [22]. Light sheathing not only serves as an enclosure but also limits the buckling of thin-walled steel studs and increases the load-carrying capacity of CFS structures. Whether the CFS shear wall can exert the material's ultimate performance depends on the sheathing material's connection strength and the CFS frame [23]. At the same time, CFS shear walls with sheathing materials can only be used in low-rise buildings, which limits the application of CFS structures in high-rise buildings.

In this study, an innovative composite wallboard made of cold-formed thin-walled C-shaped steel and multi-layer concrete, which can meet the demands of the building industry, is proposed to broaden the use of CFS structures. Two full-scale specimens were tested under cyclic load to analyze their seismic performance, including failure mode, hysteresis and skeleton curves, strength and stiffness degradation, ductility, and energy dissipation capacity. Additionally, using the software ABAQUS, the nonlinear finite element (FE) model was established and used to understand the structures' seismic performance better. This study will promote the wider use of CFS structures in high-rise buildings.

2. Construction of the New Composite Wallboard

With increasingly severe population aging and labor shortages, prefabricated buildings have been the primary selection of the building industry's transformation and upgrading,

the aims of which are to be highly industrialized, have low-carbon emissions, and be sustainable and environmentally friendly [24,25]. To meet the requirements of prefabricated construction and improve the integrity and thermal insulation performance of wallboard, this study proposes a new type of composite multi-layer concrete wallboard, as shown in Figure 1. It can be seen that the composite wallboard is composed of four parts: a fine aggregate concrete layer, a cold-formed thin-walled C-shaped steel frame welded with reinforcement mesh and wire mesh, a foam concrete layer, and a cement mortar layer. The composite wallboard can be used independently as a shear wall in low-rise buildings and can also be connected with a steel frame in high-rise buildings as an exterior shear wall.

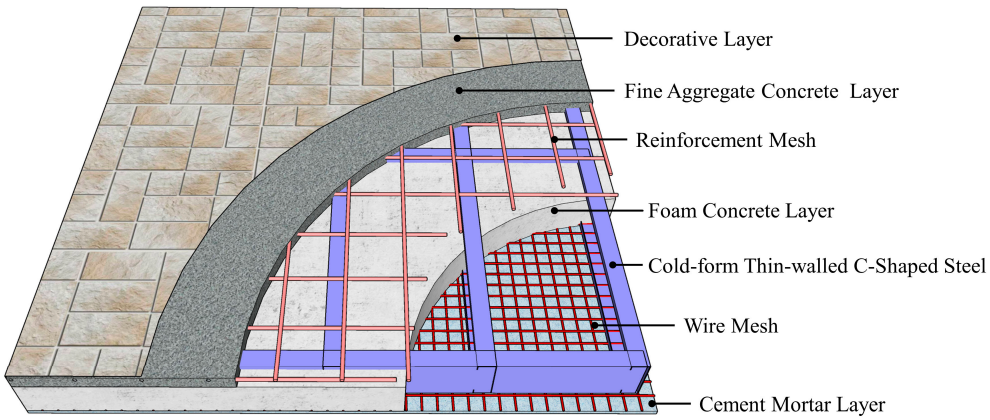

Figure 1. Diagram of the composite wallboard.

The following is how the composite wallboard is made:

(1) Erect the side formwork on the formwork platform according to the size of the wallboard, lay the decorative materials on the formwork counter, and spray polymer mortar with a thickness of 3–5 mm;

(2) Weld the cold-formed thin-walled C-shaped steel into a frame, and weld reinforcement mesh on one side and wire mesh on the other side of the CFS frame; then, lift it into the formwork;

(3) Pour fine aggregate concrete into the formwork and vibrate it tightly, subsequently pouring foam concrete into the formwork;

(4) After the initial setting of the foamed concrete, the surface is plastered with 10–15 mm cement mortar and pressed into alkali-resistant glass fiber;

(5) Dismantle the side formwork and autoclave the wallboard for curing.

Compared to traditional CFS shear walls with sheathing materials, the manufacturing of composite wallboard can be produced in factories at assembly lines, ensuring the precision and production quality of the components and meeting the requirements of the construction industry. The C-shaped steel mainly bears the axial load, and the fine aggregate concrete layer provides the lateral stiffness of the wallboard. Foam concrete acts as a filling material due to its effective thermal insulation and ability to withstand fires. Meanwhile, related studies have shown that, due to the interaction between C-shaped steel and foam concrete, foam concrete is considered effective in restraining the early local buckling of C-shaped steel under compression [26,27]. Cement mortar serves as an interior surface layer to facilitate interior decoration. Reinforcement mesh and wire mesh help to improve the bond strength of C-shaped steel to the fine aggregate concrete and cement mortar and enhance the integrity of the wallboard.

3. Experiments

3.1. Specimen Design

In order to investigate the cyclic performance of steel-frame composite wallboard shear walls, two specimens, numbered WP-1 and WP-2, were designed with the connection method as the parameter. The dimensions of the steel-frame composite wallboard shear

wall, the arrangement of the angle steel connector, and the C-shaped steel of the composite wallboard are shown in Figure 2. The composite wallboard in the WP-1 test piece was welded with the steel frame through the extended C-shaped steel and the angle steel connectors with the beam (shown in yellow); WP-2 had added angle steel connectors with the column (shown in red) compared with WP-1.

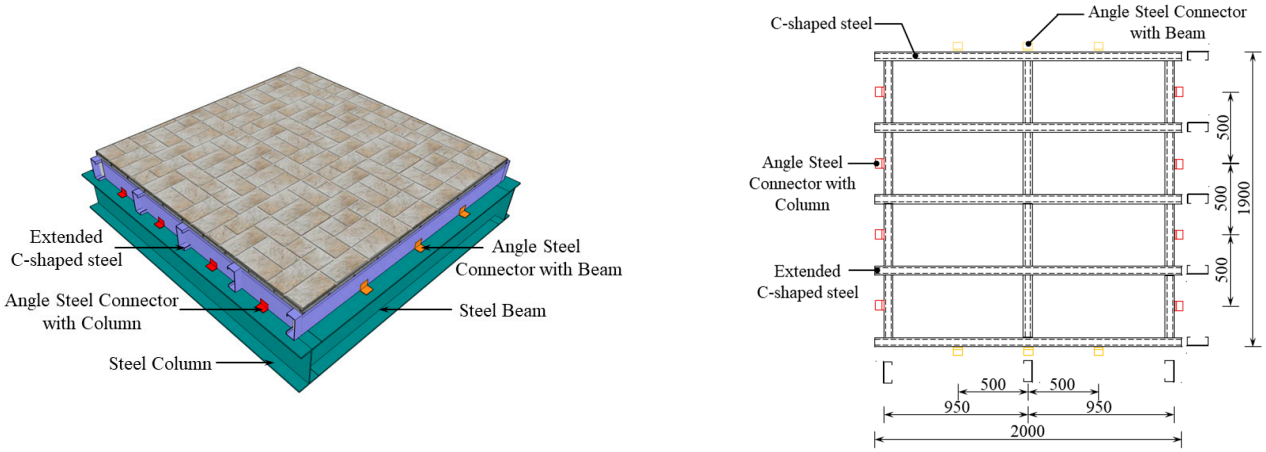

Figure 2. The structure (**a**) the steel-frame composite wallboard shear wall; (**b**) the arrangement of the angle steel connector and the C-shaped steel of the composite wallboard.

Figure 3 depicts the composite wallboard's cross-section. The thickness of the composite wallboard is 210 mm, of which the thicknesses of the fine aggregate concrete layer, cement mortar layer, and foam concrete layer are 50, 10, and 140 mm, respectively. The cross-sectional dimensions of the C-shaped steel were 160 × 60 × 20 × 2.5 mm, and both sides of the C-shaped steel were welded with a reinforcement mesh diameter of 6 mm and a spacing of 200 mm and a wire mesh diameter of 3 mm and a spacing of 50 mm. The strength grade of the fine aggregate concrete layer was C20, and the density of the foam concrete was 500 kg/m^3. The steel frame was made of a hot-rolled H-beam where the cross-sectional dimensions, $h \times b \times t_b \times t_f$, were 300 × 150 × 6.5 × 9 mm. The parameters of the components of the specimen are shown in Table 1.

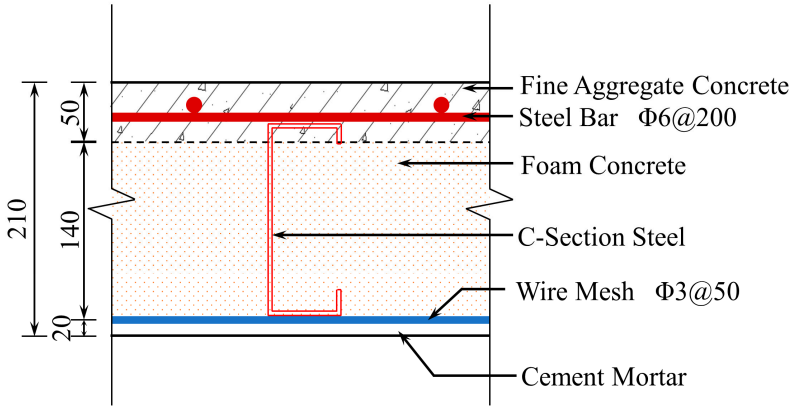

Figure 3. Cross-section of the composite wallboard.

3.2. Material Properties

3.2.1. The Steel

The specimens for the tensile material properties test were made according to the relevant requirements GB/T 2975-2018 [28], and the material properties test results of each section of the specimens are shown in Table 2. The two letters in the name of the

sample represent the name of the sampling location, where CS stands for C-section steel, AS stands for angle steel, FS stands for Flange steel, WS stands for Web steel, and the number represents the thickness of the sample; t is the actual thickness, f_y and f_u are the yield and ultimate strength, respectively, and u is the yield ratio of the sample. The elastic modulus of the steel is 205 GPa.

Table 1. Parameters of the component.

Component	Section Type	Sectional Dimension (mm)	Steel Grade
Steel Column	Hot-rolled H-shaped	300 × 150 × 6.5 × 9	Q235
Steel Beam	Hot-rolled H-shaped	300 × 150 × 6.5 × 9	Q235
Cold-formed Thin-walled Steel	C-shaped	160 × 60 × 20 × 2.5	Q235
Connector with beam	Hot-rolled equilateral angle	50 × 5	Q235
Connector with column	Hot-rolled equilateral angle	40 × 4	Q235

Table 2. The material properties of the steel as used here.

Location	Sample	t (mm)	f_y (Mpa)	f_u (Mpa)	u
C-shaped Steel	CS-2	2.5	321.7	431.2	0.75
Wire Mesh	WM-3	3.0	270.1	366.1	0.74
Reinforcement Mesh	RM-6	6.0	348.7	469.5	0.74
Angle Steel	AS-4	4.0	340.7	473.3	0.72
	AS-5	5.0	336.2	465.0	0.72
Flange	FS-9	9.0	326.5	475.0	0.69
Web	WS-6	6.5	353.4	457.5	0.77

3.2.2. The Concrete

In accordance with the Chinese standard GB/T 50081-2019 [29], the test block was a 150 mm cube, as shown in Figure 4. The test blocks and test pieces were poured at the same time and cured under the same conditions. Table 3 describes the mix proportion and material test results of fine aggregate concrete, cement mortar, and foam concrete.

Figure 4. Foam concrete samples.

Table 3. The mechanical properties of the concrete.

Materials	Mix Proportion (kg/m^3)					Cube Compressive Strength (Mpa)
	Water	Cement	Sand	Gravel	Foaming Agent	
Fine aggregate concrete	213	419	652	1061	-	17.5
Cement mortar	310	200	1450	-	-	3.7
Foam concrete	612	507	-	-	1.8	2.0

3.3. The Test Device and the Measurement Scheme

The low-cycle reciprocating loading test device for the specimen is shown in Figure 5. A rigid ground beam was fastened to the ground with anchor bolts, and the steel frame

was attached to it by bolts. A lateral restraint device was set on the reaction frame, which restrained the steel frame's out-of-plane deformation through pulleys, to prevent the steel frame from out-of-plane instability and damage during loading.

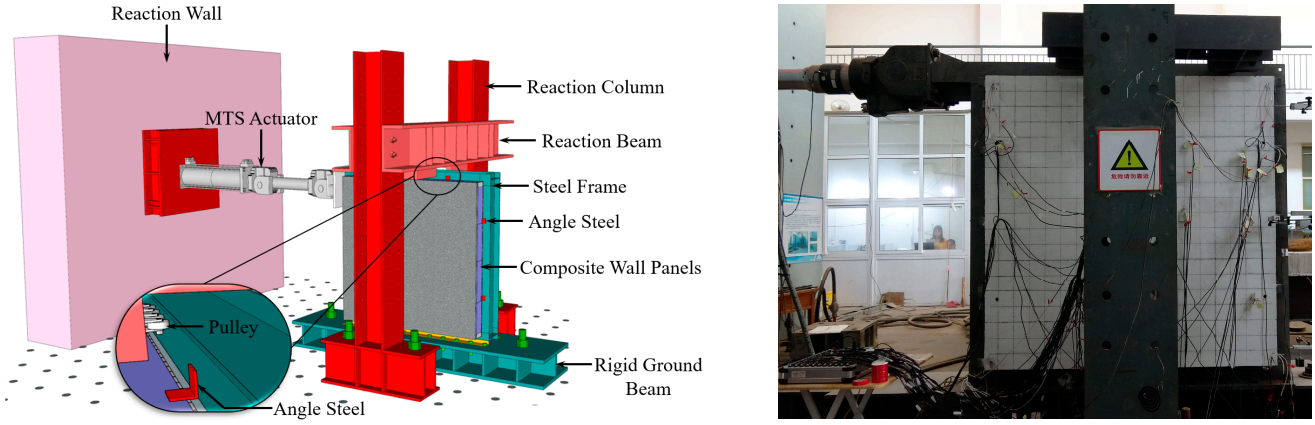

Figure 5. Schematic and test photos of loading devices: (**a**) schematic figure; (**b**) test photos.

The measurements included the specimen's lateral displacement, the loading point's force and displacement, and the strain distribution in the C-shaped steel and fine aggregate concrete. The arrangement of the linear variable displacement transducer (LVDT) and the strain gauge of each component are shown in Figure 6. The actuator and LVDT automatically collect the loading point's force and displacement. The static strain collector measures each component's strain distribution in the core area of the node.

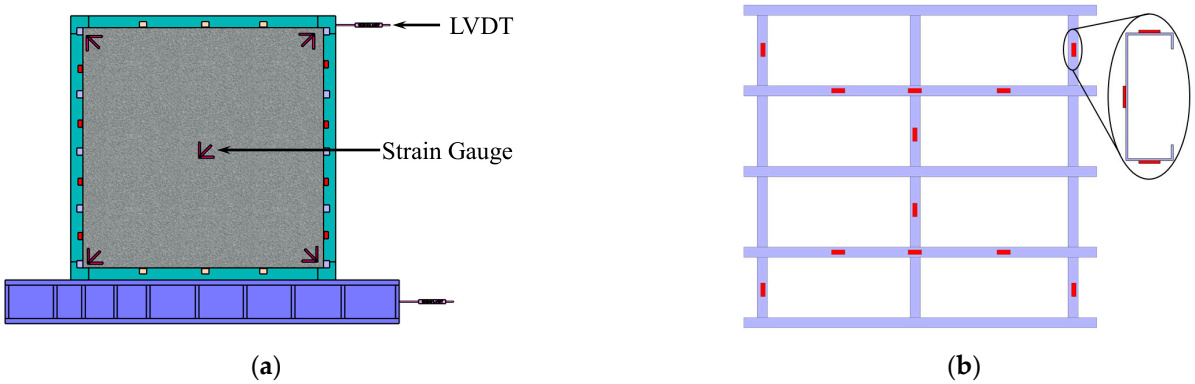

Figure 6. Schematic of the measurement layout: (**a**) the arrangement of strain gauges on the composite wallboard; (**b**) the arrangement of strain gauges on the C-shaped steel.

3.4. The Loading Scheme

The force-displacement hybrid control approach was chosen in this paper. The loading protocol is shown in Figure 7. The first-to-third displacement levels were performed in load control mode, with one cycle applied at each displacement level. Displacement control mode was used starting from the fourth displacement cycle, with three cycles applied at each displacement level. The displacement level increased with increasing yield displacement. It was found that the Δy of the specimens was about 6 mm. In the load control phase, the loading rate was 1 kN/s, and the displacement control phase was 0.5 mm/s. The test was terminated when the composite wallboard was damaged or the bearing capacity dropped below 80% of the ultimate bearing capacity.

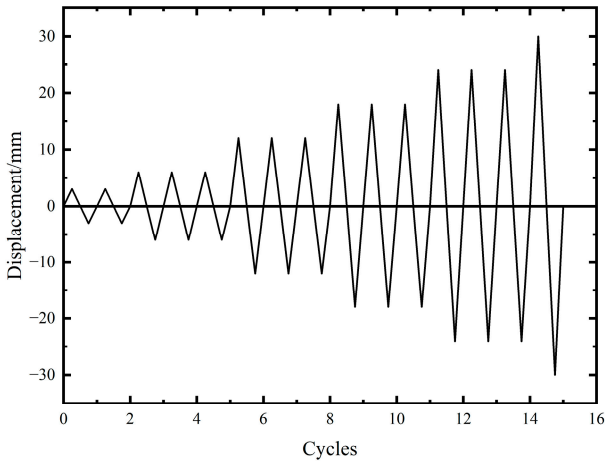

Figure 7. Loading protocol.

4. Test Results and Analyses

4.1. Test Phenomena and Failure Modes

(1) WP-1

When the loading displacement was within 12 mm, there was no crack on the mortar and concrete surface, and the specimen was in the elastic stage. When the loading displacement reached 24 mm, 45° cracks appeared in the middle area of the mortar layer, and a vertical crack emerged at the junction between the side of the concrete layer and the C-shaped steel. When the loading displacement reached 30 mm, in the middle area of the fine aggregate concrete layer, 45° cracks appeared, and the vertical cracks extended upward. With the increase in displacement, the number and width of diagonal cracks in the cement mortar layer and the concrete layer increased. When the controlled displacement reached 42 mm, the lower corners of the mortar layer peeled off, exposing the skeleton, and the filler materials inside the wallboard fell off, as shown in Figure 8a. When the loading displacement reached 84 mm, the lower part of the mortar layer became warped, and the concrete layer peeled off the wallboard. When the controlled displacement reached 90 mm, the force dropped to 80% of the ultimate bearing capacity. At this time, some extended C-shaped steel welds were torn. When the displacement reached 102 mm, the load dropped to 80% of the maximum load, and the test was completed. The failure mode of WP-1 after loading is shown in Figure 8b.

(**a**) (**b**)

Figure 8. Damage to the WP-1 specimen: (**a**) the stripping of the fine aggregate concrete layer and C-shaped steel; (**b**) the failure mode after loading.

(2) WP-2

When the loading displacement reached 12 mm, vertical cracks emerged in the lower part of the side of the concrete layer. When the loading displacement reached 18 mm, a 45° inclined crack appeared in the middle of the mortar layer. When the loading displacement reached 30 mm, the surface of the concrete layer had 45° inclined cracks, the vertical cracks on the side of the concrete layer gradually extended upward with the loading, as shown in Figure 9a, and the cracks on the mortar layer gradually increased with the loading. When the loading displacement reached 42 mm, a loud noise was heard during the loading process, and the lower part of the concrete layer rose. When the loading displacement reached 54 mm, the lower part of the mortar layer began to peel, and the internal foam concrete started to fall off. When the loading displacement reached 78 mm, the concrete layer peeled off, the force declined to 80% of the peak load, and the loading ended. The failure mode of WP-2 after loading is shown in Figure 9b.

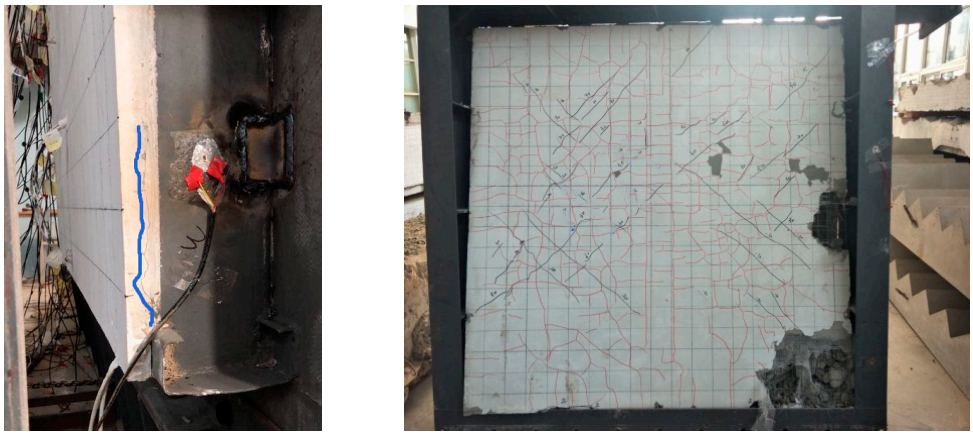

(**a**) (**b**)

Figure 9. Damage to the WP-2 specimen: (**a**) vertical cracks; (**b**) the failure mode after loading.

The above tests show that during the loading process, the cement mortar layer and the fine aggregate concrete layer of the composite wallboard had successive diagonal cracks. Then, the interface between the C-shaped steel and the cement mortar layer had separation cracks. The corners of the cement mortar layer and fine aggregate concrete layer were crushed, the fine aggregate concrete layer and the skeleton peeled off, and the carrying capacity dropped significantly. When the specimen was damaged, dense inclined 45° cracks appeared in the cement mortar and the fine aggregate concrete layers. The composite wallboard had the characteristics of shear failure. The difference between the two test pieces was that the connecting weld between the extended C-shaped steel and the steel frame of WP-1 was damaged, while the connecting weld of the WP-2 test piece was not damaged due to the increase in the number of connectors.

4.2. The Hysteresis Curves

The hysteresis curves of the WP-1 and WP-2 specimens are shown in Figure 10. The hysteresis curves of the two specimens are similar in shape, showing the inverse "S" shape, which is related to the shear damage of the composite wallboard. However, the area surrounded by the hysteresis loop is large, and the specimens have good energy dissipation capacity.

In the elastic phase, the load–displacement curve is linear, the hysteresis loop's surrounding area is smaller, and the energy dissipation capacity of the sample can be neglected.

Cracks emerged and developed in the mortar and concrete layers as the displacement increased. The lateral stiffness contributed by the composite wallboard gradually decreased, the load–displacement curve entered the nonlinear stage, the load gradually increased, and

the hysteresis loop's surrounding area increased. The specimen consumed energy through the deformation of the composite plate and the steel frame.

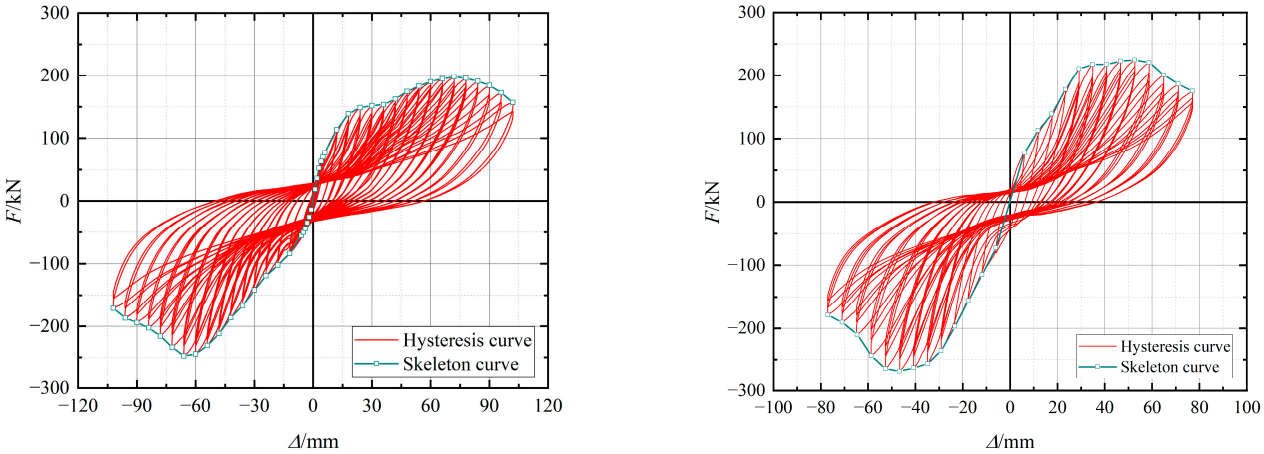

Figure 10. The hysteresis curves: (**a**) WP-1; (**b**) WP-2.

In the damage phase, the corner of the fine aggregate concrete layer was crushed under the action of the oblique pressure zone, and the bearing capacity of the specimen was reduced. In contrast, the cement mortar layer and the fine aggregate concrete layer were detached from the C-shaped steel, and the synergistic working performance of the composite wallboard was reduced. The deformation of the steel frame and the composite wallboard was not consistent, resulting in the pinching of the hysteresis curve.

4.3. The Skeleton Curve

The envelope of the load–displacement hysteresis curve obtained by the repeated load test is called the skeleton curve. Figure 11 displays the skeleton curves of the WP-1 and WP-2 specimens.

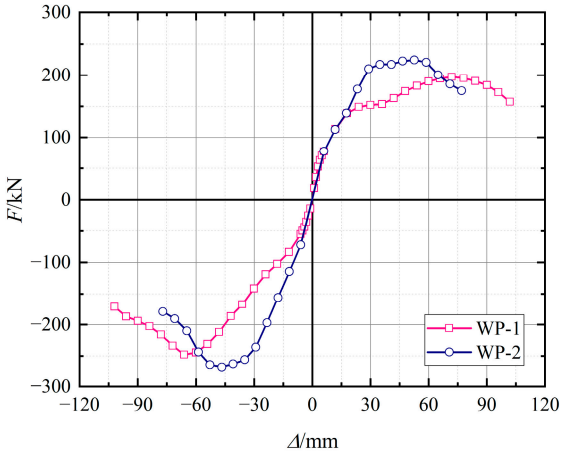

Figure 11. The skeleton curves of WP-1 and WP-2.

The skeleton curves of both specimens are "S"-shaped, indicating that the specimens have gone through three stages: elasticity, elastoplasticity, and damage degradation. The stiffness of the two models is the same at the elastic stage, and the skeleton curves overlap. As the deformation increased, cracks appeared and developed in the cement mortar and fine aggregate concrete layers one after another, which led to a decrease in the stiffness and slope of the skeleton curve. However, due to the higher connection strength between the composite wallboard and the steel frame of the WP-2 specimen, the wall plate participated

in the deformation to a greater extent; the lateral stiffness of WP-2 in the elastic-plastic stage was higher than that of WP-1, and the slope of the skeleton curve was greater. The specimen had reached the ultimate bearing capacity with the breaking and falling off of the cement mortar layer and the fine aggregate concrete layer.

The bearing capacity of WP-1 reached the positive peak load of 197.40 kN, where the forward displacement reached 71.96 mm, and the bearing capacity reached the negative peak load of 247.99 kN, where the negative displacement reached 66.04 mm. When the positive loading displacement reached 52.65 mm, the bearing capacity of WP-2 reached a peak load of 224.75 kN, and when the negative displacement reached 46.67 mm, the bearing capacity reached a peak load of 267.99 kN. The negative bearing capacity of WP-1 and WP-2 were higher than the positive by 25.6% and 19.0%, respectively. This happened because the detachment of the fine aggregate concrete layer appeared in the lower right corner first. When the forward displacement of the wall slab occurred, it affected the formation of the compression zone in the diagonal direction of the concrete layer. Due to the higher negative ultimate bearing capacity, the crushing damage caused by the concrete layer was mainly concentrated in the lower left corner. The positive and negative peak loads of the WP-2 specimen were increased by 13.9% and 8.1%, respectively, compared with the WP-1 sample. This indicates that enhancing the connection strength between the composite wallboard and the steel frame can improve the specimen's carrying capacity and synergistic force.

When the positive loading displacement of WP-1 was in the range of 24~36 mm, the bearing capacity was unchanged with the increase in displacement, mainly due to the loosening of the lateral restraint pulley during the loading process and the out-of-plane deformation of the steel beam. After adjusting the lateral restraint device and the continuing load, the bearing capacity resumed its growth trend.

4.4. Ductility

Ductility refers to the ability of structural members to deform without a significant reduction in bearing capacity. The displacement ductility coefficient can be used for quantitative expression; the calculation formula is as follows (Equation (1)):

$$\mu = \frac{\Delta_u}{\Delta_y} \tag{1}$$

where Δ_y and Δ_u are the displacements when the specimen reaches the yield and ultimate load, respectively. This paper uses the equivalent energy elastic-plastic method with the AISI standard [30] to calculate the above values. As shown in Figure 12, the maximum load and related displacement on the envelope curves were computed at the peak point (Δ_{max}, P_{max}). The elastic point (Δ_e, P_e) is situated at 0.4 P_{max}. The secant stiffness of the load, P_e, can be used to calculate the initial lateral stiffness, k_0, and point C is the yield point. The ideal perfectly elastic-plastic bilinear model that can dissipate a comparable amount of energy (area $S_1 = S_2$) was used to arrive at the yield point (Δ_y, P_y). The 80% post-peak load was determined to be at the ultimate point (Δ_u, P_u).

Table 4 depicts the characteristic values of the test results. The positive and negative yield loads of the WP-1 specimens were 153.07 and 213.60 kN, respectively, and the negative yield load was 39.54% higher than the positive yield load. The positive and negative yielding loads of the WP-2 specimens were 203.83 and 245.09 kN, respectively, and the negative yielding load was 20.24% higher than the positive yielding load. The ductility coefficients were 2.90 and 2.38 for the WP-1 specimen in the positive and negative directions, respectively, and 2.66 and 2.59 for WP-2, respectively. The higher ductility coefficient values in the positive direction of the WP-1 specimen were mainly related to the out-of-plane deformation. In general, the displacement ductility coefficient of the steel frame-composite wallboard shear walls was around 2.6; the ductility of the specimen is not excellent, which is mainly related to the structure of the composite wallboard. After the fine aggregate concrete layer was crushed and detached from the C-shaped steel, the composite wallboard was damaged and the bearing capacity decreased rapidly.

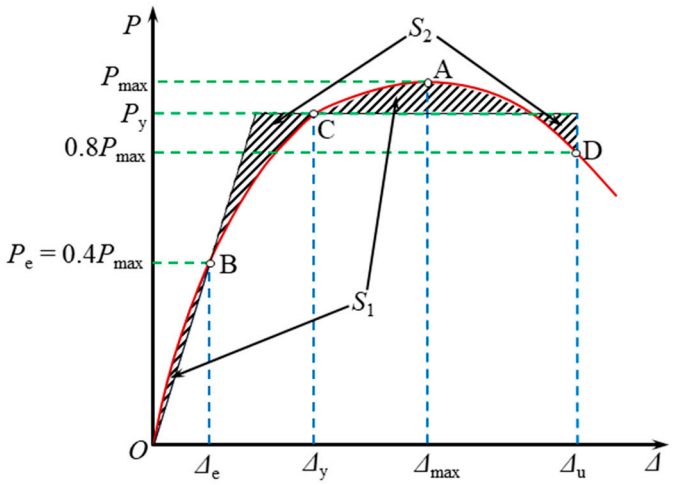

Figure 12. The characteristic values.

Table 4. The characteristic values.

Specimen	Direction	P_y (kN)	Δ_y (mm)	P_{max} (kN)	Δ_{max} (mm)	P_u (kN)	Δ_u (mm)	μ
WP-1	Positive	153.07	35.00	197.40	71.96	157.92	101.52	2.90
	Negative	213.60	36.53	247.99	66.04	198.39	86.98	2.38
	Average value	183.33	35.77	222.70	69.00	178.16	94.25	2.64
WP-2	Positive	203.83	27.93	224.75	52.65	179.80	74.23	2.66
	Negative	245.09	24.66	267.99	46.67	214.39	63.87	2.59
	Average value	224.46	26.30	246.37	49.66	197.10	69.05	2.63

4.5. Strength Degradation

Strength degradation is the process by which the displacement level stays constant while the specimen's load capacity declines over cycles. The strength degradation coefficient is denoted by λ_i and is calculated as follows (Equation (2)):

$$\lambda_i = \frac{P_j^i}{P_j^1}, \tag{2}$$

where λ_i indicates the strength degradation coefficient, $P_j{}^1$ and $P_j{}^i$ are the peak load of the first and *i*-th loading cycles at the *j*-th displacement level, respectively.

The strength degradation coefficients of the specimens are shown in Figure 13. The λ_i of the WP-1 specimen is between 0.9–1.0 and that of the WP-2 specimen is between 0.85–0.90. The specimens' strength degradation degree is not very apparent, which suggests that the bearing capacity is more stable during the loading process.

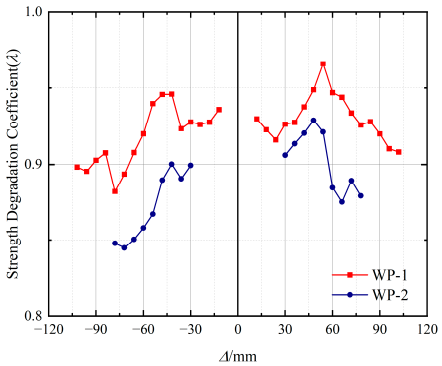

Figure 13. The strength degradation coefficient.

4.6. Rigidity Degradation

The rigidity degradation law can be expressed by the secant stiffness, K_i, under the same cycle, which is calculated as follows (Equation (3)):

$$K_j = \frac{\sum_{i=1}^{n} P_j^i}{\sum_{i=1}^{n} u_j^i}, \tag{3}$$

where P_j^i and u_j^i are the peak load and displacement of the i-th cycle at the j-th displacement level, respectively.

The equivalent stiffness of the specimen is shown in Figure 14. The initial stiffness of the WP-1 specimen was 13.96 kN/mm and that of the WP-2 specimen was 13.11 kN/mm. In the elastic stage, both connection methods can ensure the coordinated deformation of the composite wallboard and steel frame, and the ring line stiffness of the two specimens was basically the same.

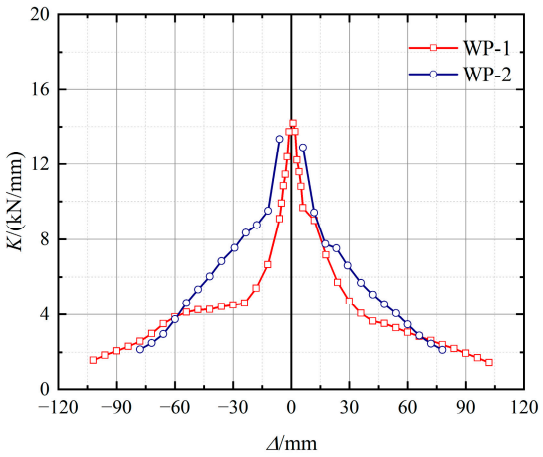

Figure 14. The rigidity degradation.

During the elastic-plastic phase, the specimens' stiffness steadily decreased as cracks developed in the mortar and concrete layers. However, the composite wall panel and steel frame in the WP-2 specimen demonstrated a better capacity for coordinated deformation due to the stronger connection between the composite wall panel and the steel frame, and the secant stiffness was higher than that of the WP-1 specimen. When the mortar layer and the concrete layer broke and fell off, the stiffness of the specimen decreased.

4.7. Energy Dissipation Capacity

The hysteresis curve's width shows the specimen's energy dissipation capacity under cyclic loading. The energy dissipation capacity is inversely proportional to the hysteresis curve width, typically expressed as the equivalent viscous damping coefficient (h_e), which is calculated as follows (Equation (4)):

$$h_e = \frac{E_d}{2\pi} = \frac{1}{2\pi}\frac{S_{ABC} + S_{CDA}}{S_{OBE} + S_{ODF}}, \tag{4}$$

where $S_{(ABC+CDA)}$ is the area enclosed by the hysteresis loop, and $S_{(OBE+ODF)}$ is the corresponding triangle's enclosed area, as shown in Figure 15. It may be concluded that the h_e values of the two specimens changed with the development of loading displacement in the same trend, both showing a trend of first increasing, then decreasing, and then slowly increasing.

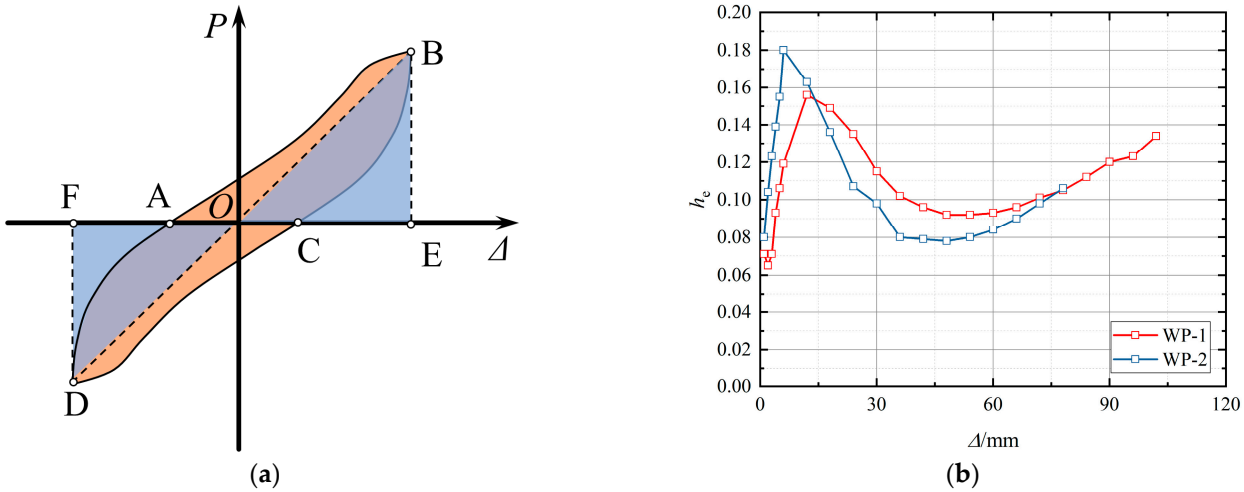

Figure 15. Energy dissipation capacity: (**a**) schematic of the hysteresis loop; (**b**) the equivalent viscous damping coefficient of the specimen.

At the early loading stage, the composite wall plate and steel frame deformed together, the hysteresis curve was full, and the equivalent viscous damping coefficient increased gradually. With the development of cracks in the cement mortar layer and concrete layer, the lateral stiffness of the specimen gradually decreased. At the same time, the hysteresis curve was pinched, and the equivalent viscous damping coefficient of the specimen gradually decreased due to the decrease in the synergistic deformation ability of the composite wall panel and steel frame after the concrete layer was detached from the C-shaped steel.

At the later loading stage, when the specimen reached the ultimate bearing capacity, the specimen stiffness was mainly provided by the steel frame, and the contribution of the composite wall plate was negligible. The steel frame mainly provided energy dissipation performance, and the equivalent viscous damping coefficient increased slowly with the increase in steel frame deformation.

Figure 16 shows the cumulative energy dissipation of the two specimens, which correspond to each level of loading displacement. It can be concluded that the steel-frame composite wallboard shear walls had qualitatively good energy dissipation capacity. The curves of the WP-1 and WP-2 specimens have similar trends, and the loading displacement is slightly higher for the WP-2 specimen than the WP-1 specimen, indicating that the enhanced connection between the composite wallboard and the steel frame can improve the energy dissipation capacity of the specimens.

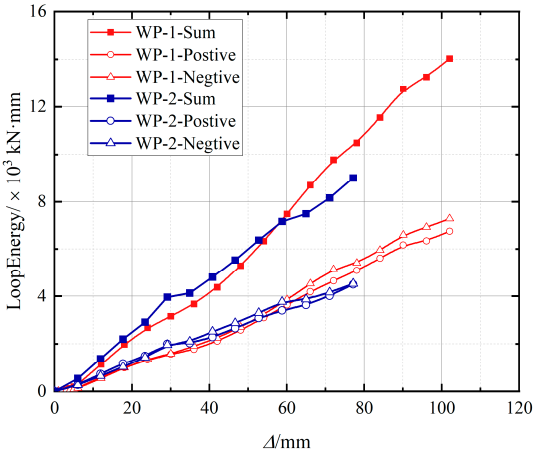

Figure 16. The loop energy of the specimen.

5. The FE Model

In order to study the seismic behavior of the steel-frame composite wallboard shear wall, finite element analyses of WP-1 and WP-2 were performed using ABAQUS/Standard. The geometry dimension, loading pattern, and boundary conditi0ons of the finite element models were all in accordance with those utilized in the experiment.

5.1. Stress–Strain Relationship

5.1.1. The Steel

The constitutive model of the steel in the FE model was established using a bilinear stress–strain relationship, which is as follows (Equation (5)):

$$\sigma_{\mathrm{i}} = \begin{cases} E_{\mathrm{s}}\varepsilon_{\mathrm{i}} & \varepsilon_{\mathrm{i}} \le \varepsilon_{\mathrm{y}} \\ f_{\mathrm{y}} + 0.01E_{\mathrm{s}}(\varepsilon_{\mathrm{i}} - \varepsilon_{\mathrm{y}}) & \varepsilon_{\mathrm{y}} < \varepsilon_{\mathrm{i}} \le \varepsilon_{\mathrm{u}} \\ f_{\mathrm{u}} & \varepsilon_{\mathrm{u}} < \varepsilon_{\mathrm{i}} \end{cases} \tag{5}$$

where σ_{i} and ε_{i} are the equivalent stress and strain, respectively; ε_{y} and ε_{u} indicate the yield and ultimate, respectively.

5.1.2. The Concrete

The concrete consists of foam concrete, fine aggregate concrete, and cement mortar, and the concrete plastic damage model was selected in ABAQUS to simulate the concrete. The foam concrete's stress–strain relationship is as follows [31] (Equations (6)–(8)):

$$y = \begin{cases} -1.041x^3 + 1.019x^2 + 1.028x - 0.017 & (0 \le x \le 1) \\ 204x^3 - 674x^2 + 737.1x - 266.1 & (1 \le x \le 1.2) \\ -0.005x^3 + 0.052x^2 - 0.211x + 0.559 & (x \ge 1.2) \end{cases} \tag{6}$$

$$x = \frac{\varepsilon}{\varepsilon_{\mathrm{fc}}} \tag{7}$$

$$y = \frac{\sigma}{f_{\mathrm{fc}}} \tag{8}$$

where f_{fc} and $\varepsilon_{\mathrm{fc}}$ represent the ultimate stress and corresponding strain of the foam concrete, respectively.

The constitutive model of fine aggregate concrete and cement mortar in compression and tension is followed by Chinese Code GB 50010-2010 [32], and the relationship in compression is as follows (Equations (9)–(14)):

$$y = \begin{cases} \alpha_{\mathrm{a}}x + (3 - 2\alpha_{\mathrm{a}})x^2 + (\alpha_{\mathrm{a}} - 2)x^3 & x \leqslant 1 \\ \frac{x}{\alpha_d(x-1)^2 + x} & x > 1 \end{cases} \tag{9}$$

$$x = \frac{\varepsilon}{\varepsilon_{\mathrm{c}}} \tag{10}$$

$$y = \frac{\sigma}{f_{\mathrm{c}}} \tag{11}$$

$$\varepsilon_{\mathrm{c}} = \left(700 + 172\sqrt{f_{\mathrm{c}}}\right) \times 10^{-6} \tag{12}$$

$$\alpha_a = 2.4 - 0.0125f_{\mathrm{c}} \tag{13}$$

$$\alpha_d = 0.157f_{\mathrm{c}}^{0.785} - 0.905 \tag{14}$$

where f_{c} and ε_{c} are the peaking stress and corresponding strain of the foam concrete, and α_{a} and α_{c} represent the calculation parameters.

In tension, the expressions for the stress–strain relationship are Equations (15)–(19):

$$y = \begin{cases} 1.2x - 0.2x^6 & x \leqslant 1 \\ \frac{x}{\alpha_t(x-1)^{1.7}+x} & x > 1 \end{cases} \quad (15)$$

$$x = \frac{\varepsilon}{\varepsilon_t} \quad (16)$$

$$y = \frac{\sigma}{f_t} \quad (17)$$

$$\varepsilon_t = f_t^{0.54} \times 65 \times 10^{-6} \quad (18)$$

$$\alpha_t = 0.312 f_t^2 \quad (19)$$

where σ_t and ε_t are the ultimate stress and strain of the concrete in tension, respectively; α_t is the calculation parameters of the descending stage. Figure 17 shows the constitutive model of steel and concrete.

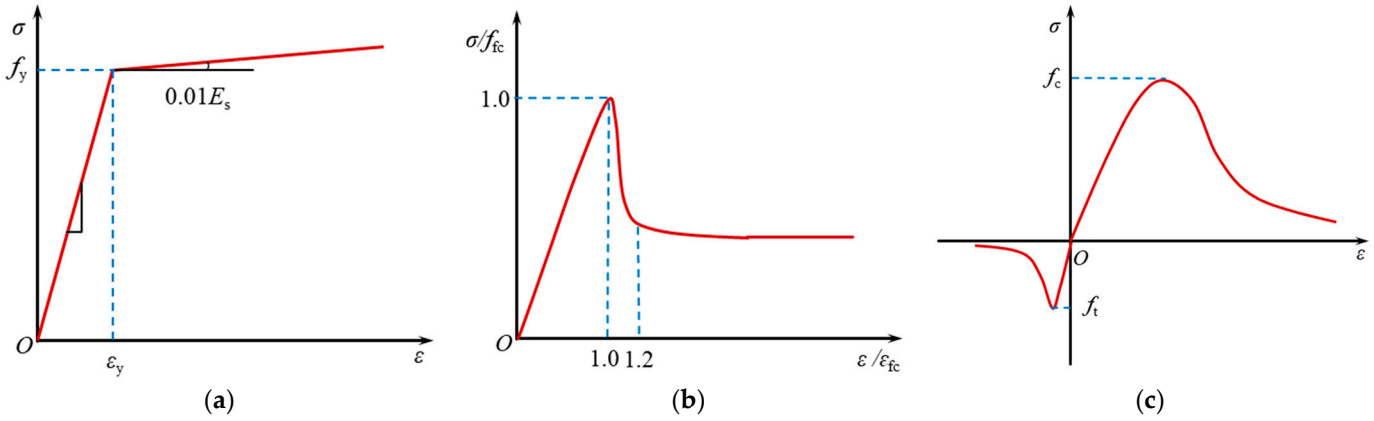

Figure 17. The constitutive model: (**a**) steel; (**b**) foam concrete; (**c**) concrete.

5.2. Element Type and Interaction

There are eight parts in the FE model, including the steel frame, the C-shaped steel, the wire mesh, the reinforcement mesh, the angle steel connector, the fine aggregate concrete, the cement mortar, and the foam concrete. The C3D8R solid element was selected to simulate the steel frame, the angle steel connector, the fine aggregate concrete, the cement mortar, and the foam concrete. Shell element S4R was used for C-shaped steel. The T3D2 truss element simulated the wire mesh and reinforcement part.

The "TIE" option was used to simulate the interaction between the fine aggregate layer, the cement mortar layer, and the foam concrete, respectively, which provided the full compatibility of the displacements. At the same time, the welding seams between the extended C-shaped steel, the angle steel connector, and the steel frame were established by the "TIE" interaction. In the production process, the wire mesh and reinforcement mesh were welded with the C-shaped steel skeleton, which can be regarded as one whole piece, so the three parts were merged into one part and "EMBEDDED" in the concrete to reduce the amount of "interaction" in the FE model.

5.3. Boundary Conditions

In the FE model, a reference point (RP) was set at the center of the top steel beam, and the reference point was coupled to the steel beam section. The loading step was to apply the reciprocal displacement at the RP. All displacement and rotation constraints were selected on the bottom steel beam to simulate the fixed boundary with the rigid beam. The top steel beam's out-of-plane displacement was restricted so that it was displaced in the loading plane to avoid torsion. The finite element model of the specimen is shown in Figure 18.

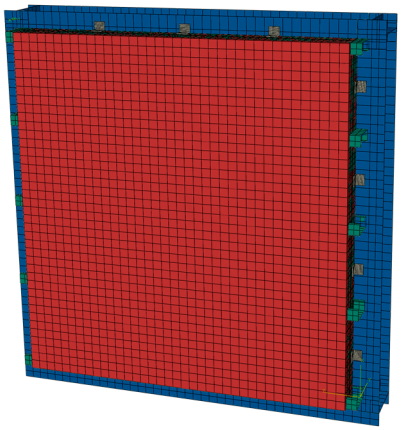

Figure 18. The finite element model.

5.4. Verification

Figure 19 compares the skeleton curves of WP-1 and WP-2 obtained from FEA with the experiment. The two curves basically coincide in the elastic stage, and the development trend in the elastic-plastic stage is consistent. However, there are clear differences between the curves in the failure stage, which may have been caused by the following reasons: the concrete layer in the finite element model was constrained by "TIE" and the "EMBEDDED" contact between the C-shaped steel skeleton and the concrete was adopted without considering the bond–slip relationship between them.

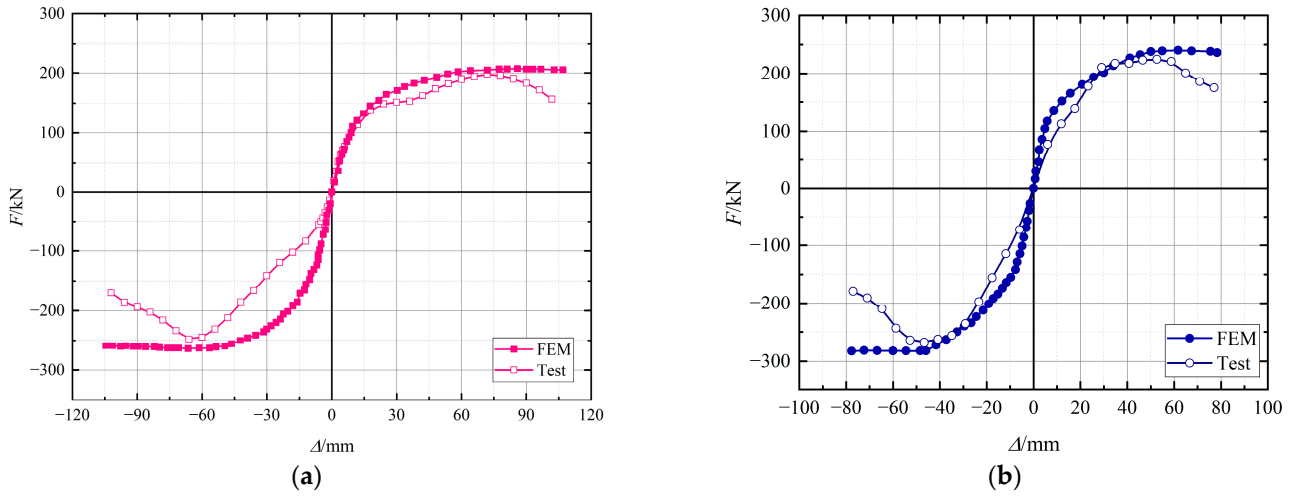

Figure 19. Comparison of the skeleton curves: (**a**) WP-1; (**b**) WP-2.

The Von Mises stress distributions of some components when WP-2 reached the ultimate load are given in Figure 20. There are stress concentrations in the bottom steel beam at the corner of the connection with the rigid beam, the stress distribution of the fine aggregate concrete is along the diagonal direction, and the stress is higher at the connection between the outreach C-shaped steel and the steel frame. All these stress distribution characteristics are close to the damage characteristics of the specimen.

Table 5 compares the yield load and bearing capacity of the specimen between the FE model and the test. The average value of the ratio of yield load calculated by the FE model to the test-measured value is 1.057, and the average value of the ratio of ultimate bearing capacity is 1.058. The standard deviation of the yield load and ultimate bearing capacity ratio is 0.084 and 0.091, respectively.

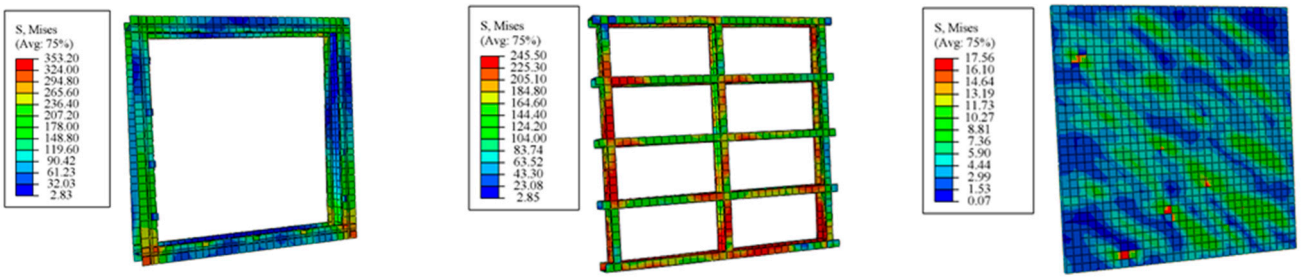

(**a**) (**b**) (**c**)

Figure 20. The Von Mises stress distribution of some parts: (**a**) steel frame; (**b**) C-shaped steel; (**c**) fine aggregate concrete.

Table 5. Load capacity comparison between the test and the FE model.

Specimen	Load Direction	$P_{y,test}$ (kN)	$P_{y,fem}$ (kN)	$P_{y,fem}/P_{y,test}$	$P_{max,test}$ (kN)	$P_{max,fem}$ (kN)	$P_{max,fem}/P_{max,test}$
WP-1	Positive	153.07	161.18	1.067	197.40	207.28	1.050
	Negative	213.60	224.49	0.964	247.99	263.07	1.061
WP-2	Positive	203.83	217.49	1.043	224.75	240.31	1.069
	Negative	245.09	259.06	1.039	267.99	282.37	1.054
			Average	1.057		Average	1.058
		Standard deviation		0.084	Standard deviation		0.091

Note: $P_{y,test}$ and $P_{y,fem}$ are the yield carrying capacity obtained from the test and the FE model, respectively; $P_{u,test}$ and $P_{u,fem}$ are the ultimate bearing capacity obtained from the test and the FE model, respectively.

Based on the above failure modes, skeleton curves, and bearing capacity comparisons, the FE model established in this study can accurately estimate the seismic behavior of steel frame-composite wallboard shear walls.

5.5. Parameter Analysis

To quantify the influence of the fine aggregate concrete layer and foam concrete layer on the bearing capacity and initial stiffness of composite wallboards, three finite element models carried out pushover analyses with WP-1 as a reference. Table 6 shows the design parameters of the FE models.

Table 6. Design parameters of the FE models.

Specimen	t_{ac} (mm)	t_{fc} (mm)	t_{mc} (mm)	t_{cw} (mm)	P_{max} (kN)	K_i (kN/mm)
WP-1	140	50	20	210	207.28	18.19
WP-3	-	-	-	-	50.74	0.87
WP-4	0	190	20	210	173.86	8.29
WP-5	190	0	20	210	340.34	67.27

Note: t_{ac} means the thickness of the fine aggregate concrete, t_{fc} is the thickness of the foam concrete, t_{mc} represents the mortar cement's thickness, t_{cw} is the thickness of the composite wallboard, and *K*i is the initial stiffness of the model.

Figure 21 represents the load–displacement curves of the FE models. The WP-3 model, consisting of the steel frame and the C-shaped steel skeleton only, had the smallest P_{max} and K_i of 50.74 kN and 0.87 kN/mm, respectively. Additionally, the P_{max} and K_i of the WP-5 model, with fine aggregate concrete instead of foam concrete, were the largest, with 340.34 kN and 67.27 kN/mm, respectively. Compared with the WP-1 model, the P_{max} and K_i of the WP-5 model increased by 64.19% and 269.82%, respectively. The P_{max} and K_i of WP-4 specimens with foam concrete instead of fine stone concrete were reduced by 16.12%

and 54.42%, respectively, compared with the WP-1 model. Therefore, the fine aggregate concrete layer provides higher lateral force resistance in the WP-1 model. At the same time, at a certain value of composite wallboard thickness, the greater the thickness of the fine aggregate concrete layer, the higher the bearing capacity and initial stiffness of the model. However, the relationship is not linear and is related to the interfacial contact between the two materials.

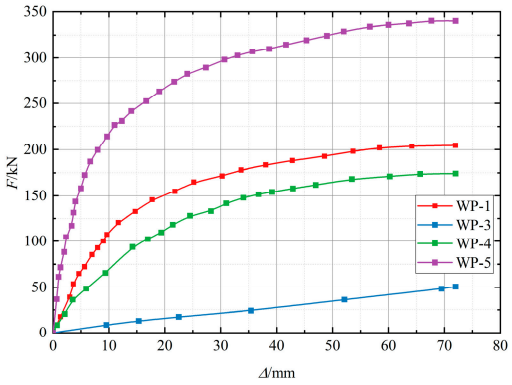

Figure 21. The load–displacement curves of the FE models.

6. Conclusions

In this study, cycling load tests of two steel-frame composite wallboard shear walls were conducted to investigate the seismic performance of the specimens. The main conclusions are as follows:

1. The specimens underwent shear damage, and the main damage characteristics of the sample were the cracking, the crushing of the cement mortar layer and fine aggregate concrete layer, and the separation from the C-shaped steel. Meanwhile, the infilled foam concrete was also crushed, and the welding seams between the extended C-shaped steel and the steel frame of the WP-1 specimen were damaged.
2. The deformations of the composite wallboard and the steel frame were not coordinated after the composite wallboard was damaged, resulting in a clear "pinch" effect in the hysteresis curves of the two specimens. The average ultimate bearing capacity of WP-2 in positive and negative directions was 10.6% higher than that of WP-1, indicating that enhancing the connection strength between the composite wallboard and the steel frame improves synergistic deformation and increases the bearing capacity of the specimens. The negative bearing capacity of the WP-1 and WP-2 specimens was 25.6% and 19.0% higher than the positive bearing capacity, respectively, which is related to the damaged position of the concrete layer.
3. The displacement ductility coefficient of the specimen was around 2.6, and the ductility was not excellent, which was mainly related to the structure of the composite wallboard. The strength degradation coefficient was within the range of 0.85–1.0 during loading, which indicated that the bearing capacity was stable.
4. The ratios of the yield and ultimate bearing capacity of the WP-1 and WP-2 specimens, calculated by the FE model to the measured values, were 1.057 and 1.058, respectively. The finite element model established can accurately estimate the seismic behavior of steel-frame composite wallboard shear walls.
5. Parametric analysis shows that in the WP-1 model, the fine aggregate concrete layer provides higher lateral force resistance, and the greater the thickness of the fine aggregate concrete layer, the higher the bearing capacity and initial stiffness of the model.

Finally, it should be understood that this study is only a preliminary attempt to apply composite wallboards as a shear wall structure to steel frames. Before being applied to actual projects, there is still some work to be done, such as finding a reasonable thickness for each layer of the concrete, the improvement of the connection between the composite

wallboard and the steel frame, and the consideration of the interaction between different layers of concrete.

Author Contributions: Conceptualization, X.J. and Z.W.; methodology, Z.L., J.-B.Y. and L.H.; writing—original draft preparation, Z.W.; writing—review and editing, Z.W.; supervision, Z.L. All authors have read and agreed to the published version of the manuscript.

Funding: This research was funded by the National Key Research and Development Program of China, grant number SQ2020YFF0426523; the Major Scientific and Technological Innovation Projects of Shandong Province, grant number 2021CXGC011204; the Natural Science Foundation of Shandong Province, grant number ZR2020QE247; the Research and Development Project of the Housing and Urban–Rural Development of Shandong Province, grant number 2021-K5-14; and the Research Fund for the Doctoral Program of Shandong Jianzhu University, grant number X19035Z.

Data Availability Statement: Not applicable.

Conflicts of Interest: The authors declare no conflict of interest.

References

1. Rahnavard, R.; Craveiro, H.D.; Lopes, M.; Simões, R.A.; Laím, L.; Rebelo, C. Concrete-Filled Cold-Formed Steel (CF-CFS) Built-up Columns under Compression: Test and Design. *Thin-Walled Struct.* **2022**, *179*, 109603. [CrossRef]
2. Hasanali, M.; Roy, K.; Mojtabaei, S.M.; Hajirasouliha, I.; Clifton, G.C.; Lim, J.B.P. A Critical Review of Cold-Formed Steel Seismic Resistant Systems: Recent Developments, Challenges and Future Directions. *Thin-Walled Struct.* **2022**, *180*, 109953. [CrossRef]
3. Shamim, I.; Rogers, C.A. Steel Sheathed/CFS Framed Shear Walls under Dynamic Loading: Numerical Modelling and Calibration. *Thin-Walled Struct.* **2013**, *71*, 57–71. [CrossRef]
4. Balh, N.; DaBreo, J.; Ong-Tone, C.; El-Saloussy, K.; Yu, C.; Rogers, C.A. Design of Steel Sheathed Cold-Formed Steel Framed Shear Walls. *Thin-Walled Struct.* **2014**, *75*, 76–86. [CrossRef]
5. Badr, A.R.; Elanwar, H.H.; Mourad, S.A. Numerical and Experimental Investigation on Cold-Formed Walls Sheathed by Fiber Cement Board. *J. Constr. Steel Res.* **2019**, *158*, 366–380. [CrossRef]
6. Sonkar, C.; Bhattacharyya, S.K.; Mittal, A.K. Investigations on Cold-Formed Steel Wall Panels with Different Sheathing Boards under Axial Loading: Experimental and Analytical/Semi-Analytical Studies. *J. Build. Eng.* **2021**, *44*, 102924. [CrossRef]
7. Xu, Y.; Zhou, X.; Shi, Y.; Zou, Y.; Xu, L.; Xiang, Y. Ke Ke Lateral Resistance of OSB Sheathed Cold-Formed Steel Shear Walls. *Thin-Walled Struct.* **2021**, *161*, 107451. [CrossRef]
8. Ye, J.; Wang, X.; Jia, H.; Zhao, M. Cyclic Performance of Cold-Formed Steel Shear Walls Sheathed with Double-Layer Wallboards on Both Sides. *Thin-Walled Struct.* **2015**, *92*, 146–159. [CrossRef]
9. Lin, S.-H.; Pan, C.-L.; Hsu, W.-T. Monotonic and Cyclic Loading Tests for Cold-Formed Steel Wall Frames Sheathed with Calcium Silicate Board. *Thin-Walled Struct.* **2014**, *74*, 49–58. [CrossRef]
10. Attari, N.K.A.; Alizadeh, S.; Hadidi, S. Investigation of CFS Shear Walls with One and Two-Sided Steel Sheeting. *J. Constr. Steel Res.* **2016**, *122*, 292–307. [CrossRef]
11. DaBreo, J.; Balh, N.; Ong-Tone, C.; Rogers, C.A. Steel Sheathed Cold-Formed Steel Framed Shear Walls Subjected to Lateral and Gravity Loading. *Thin-Walled Struct.* **2014**, *74*, 232–245. [CrossRef]
12. Mohebbi, S.; Mirghaderi, S.R.; Farahbod, F.; Bagheri Sabbagh, A.; Torabian, S. Experiments on Seismic Behaviour of Steel Sheathed Cold-Formed Steel Shear Walls Cladded by Gypsum and Fiber Cement Boards. *Thin-Walled Struct.* **2016**, *104*, 238–247. [CrossRef]
13. Zeynalian, M.; Ronagh, H.R. Seismic Performance of Cold Formed Steel Walls Sheathed by Fibre-Cement Board Panels. *J. Constr. Steel Res.* **2015**, *107*, 1–11. [CrossRef]
14. Serrette, R.L.; Encalada, J.; Juadines, M.; Nguyen, H. Static Racking Behavior of Plywood, OSB, Gypsum, and FiberBond Walls with Metal Framing. *J. Struct. Eng.* **1997**, *123*, 1079–1086. [CrossRef]
15. Liu, P.; Peterman, K.D.; Schafer, B.W. Impact of Construction Details on OSB-Sheathed Cold-Formed Steel Framed Shear Walls. *J. Constr. Steel Res.* **2014**, *101*, 114–123. [CrossRef]
16. Karabulut, B.; Soyoz, S. Experimental and Analytical Studies on Different Configurations of Cold-Formed Steel Structures. *J. Constr. Steel Res.* **2017**, *133*, 535–546. [CrossRef]
17. Abeysiriwardena, T.; Mahendran, M. Numerical Modelling and Fire Testing of Gypsum Plasterboard Sheathed Cold-Formed Steel Walls. *Thin-Walled Struct.* **2022**, *180*, 109792. [CrossRef]
18. Liu, B.; Hao, J.-P.; Zhong, W.-H.; Wang, H. Performance of Cold-Formed-Steel-Framed Shear Walls Sprayed with Lightweight Mortar under Reversed Cyclic Loading. *Thin-Walled Struct.* **2016**, *98*, 312–331. [CrossRef]
19. Xu, Z.; Chen, Z.; Yang, S. Seismic Behavior of Cold-Formed Steel High-Strength Foamed Concrete Shear Walls with Straw Boards. *Thin-Walled Struct.* **2018**, *124*, 350–365. [CrossRef]
20. Zhang, X.; Zhang, E.; Li, C. Study on Axial Compression Mechanical Behavior of Cold-Formed Thin-Walled C-Shaped Steel Composite Wall Sheathed with Straw Board on Both Sides. *Structures* **2021**, *33*, 3746–3756. [CrossRef]

21. Wu, H.; Sui, L.; Zhou, T.; Lu, L.; Li, X. Estimation of Lateral Stiffness for Gypsum-Filled Cold-Formed Steel Shear Walls. *Structures* **2021**, *32*, 28–37. [CrossRef]
22. Shakibanasab, A.; Attari, N.K.A.; Salari, M. A Statistical and Experimental Investigation into the Accuracy of Capacity Reduction Factor for Cold-Formed Steel Shear Walls with Steel Sheathing. *Thin-Walled Struct.* **2014**, *77*, 56–66. [CrossRef]
23. Othuman Mydin, M.A.; Wang, Y.C. Structural Performance of Lightweight Steel-Foamed Concrete–Steel Composite Walling System under Compression. *Thin-Walled Struct.* **2011**, *49*, 66–76. [CrossRef]
24. Tumminia, G.; Guarino, F.; Longo, S.; Ferraro, M.; Cellura, M.; Antonucci, V. Life Cycle Energy Performances and Environmental Impacts of a Prefabricated Building Module. *Renew. Sustain. Energy Rev.* **2018**, *92*, 272–283. [CrossRef]
25. Minunno, R.; O'Grady, T.; Morrison, G.; Gruner, R.; Colling, M. Strategies for Applying the Circular Economy to Prefabricated Buildings. *Buildings* **2018**, *8*, 125. [CrossRef]
26. Prabha, P.; Marimuthu, V.; Saravanan, M.; Palani, G.S.; Lakshmanan, N.; Senthil, R. Effect of Confinement on Steel-Concrete Composite Light-Weight Load-Bearing Wall Panels under Compression. *J. Constr. Steel Res.* **2013**, *81*, 11–19. [CrossRef]
27. Hegyi, P.; Dunai, L. Experimental Investigations on Ultra-Lightweight-Concrete Encased Cold-Formed Steel Structures. *Thin-Walled Struct.* **2016**, *101*, 100–108. [CrossRef]
28. *GB/T 2975-2018*; Steel and Steel Products-Location and Preparation of Samples and Test Pieces for Mechanical Testing, Chinese National Standard. Standards Press of China: Beijing, China, 2018.
29. *GB/T 50081-2019*; Standard for Test Methods of Concrete Physical and Mechanical Properties, Chinese National Standard. Standards Press of China: Beijing, China, 2019.
30. *AISI S213*; North American Standard for Cold-Formed Steel Framing-Lateral Design. American Iron and Steel Institute(AISI): Washington, DC, USA, 2007.
31. Liu, D.; Fu, F.; Liu, W. Structural Behavior of Composite Floor System Using Cold-Formed Thin-Walled C Steel Channel Embedded Foam Concrete. *Appl. Sci.* **2021**, *11*, 9888. [CrossRef]
32. *GB/T 50010-2010*; Code for Design of Concrete Structures, Chinese National Standard. Standards Press of China: Beijing, China, 2015.